New Journal of Physics
The open-access journal for physics

Single-mode electrically pumped GaSb-based VCSELs emitting continuous-wave at 2.4 and 2.6 μm

Alexander Bachmann[1], **Shamsul Arafin and Kaveh Kashani-Shirazi**
Walter Schottky Institut, Technische Universität München, Am Coulombwall 3, 85748 Garching, Germany
E-mail: bachmann@wsi.tum.de

New Journal of Physics **11** (2009) 125014 (17pp)
Received 30 June 2009
Published 17 December 2009
Online at http://www.njp.org/
doi:10.1088/1367-2630/11/12/125014

Abstract. Vertical-cavity surface-emitting lasers (VCSELs) are perfect light sources for spectroscopic applications, where properties such as continuous-wave (cw) operation, single-mode emission, high lifetime and often low power consumption are crucial. For applications such as tunable diode laser absorption spectroscopy (TDLAS), there is a growing interest in laser devices emitting in the near- to mid-infrared wavelength range, where many environmentally and technologically important gases show strong absorption lines. The (AlGaIn)(AsSb) material system based on GaSb is the material of choice for covering the 2.0–3.3 μm range. In this paper, we report on electrically pumped single-mode VCSELs with emission wavelengths of 2.4 and 2.6 μm, operating cw at room temperature and beyond. By (electro-) thermal tuning, the emission wavelength can be tuned mode-hop free over a range of several nanometers. In addition, low threshold currents of several milliamperes promise mobile application. In the devices, a structured buried tunnel junction with subsequent overgrowth has been used in order to achieve efficient current confinement, reduced optical losses and increased electrical conductivity. Furthermore, strong optical confinement is introduced in the lasers due to laterally differing cavity lengths.

[1] Author to whom any correspondence should be addressed.

© IOP Publishing Ltd and Deutsche Physikalische Gesellschaft

Contents

1. Introduction **2**
2. BTJ **3**
3. Device design and fabrication **5**
3.1. Device structure 5
3.2. Fabrication 6
3.3. Optical properties 7
4. Results **10**
4.1. VCSELs emitting at 2.4 μm 10
4.2. VCSELs emitting at 2.6 μm 14
5. Conclusion and outlook **15**
Acknowledgments **16**
References **16**

1. Introduction

Since the development of the first semiconductor lasers in 1962 by Robert Hall [1], these devices have undergone a rapid improvement, which has led to highly reliable, efficient low-cost components with high beam quality. Their applications include optical data storage, data transmission, distance measurement, high precision medical surgery and sensing. Unlike the commonly known and market dominating edge-emitting structures that emit light perpendicular to the epitaxial growth direction of the semiconductor layers, the so-called vertical-cavity surface-emitting lasers (VCSELs) feature surface emission parallel to the growth direction. This concept, proposed by Iga in 1977 [2] and firstly realized two years later [3], offers numerous advantages, such as low power consumption, low beam divergence, high fiber coupling efficiency due to a circular output beam, on-wafer testing capability and low-cost potential. Furthermore, these devices emit inherently longitudinally single-mode due to their small cavity lengths of only several micrometers and, therefore, large longitudinal mode separation. Consequently, their development has been pushed forward and devices entered industrial applications, such as optical data transmission or implementation in laser mice for personal computers. Their beneficial spectral properties make these lasers also ideally suited for sensing applications. For security and environmental purposes, the detection of hazardous gases has gained increasing attention over the last couple of years. Compared to conventionally used systems based on electrochemical sensors, tunable diode laser absorption spectroscopy (TDLAS) offers tremendous benefits for the detection of gases, such as rapid response time, long-term stability, high selectivity and sensitivity. This method uses the fact that numerous gases have strong absorption lines in the near- to mid-infrared spectral range. These molecule resonances cause characteristic 'fingerprints' in the detected light versus current (L–I)-characteristics of the laser, as the laser's wavelength tunes over several nanometers while changing the bias current and therefore light is absorbed if the resonance is hit. By analyzing these dips in the L–I-characteristics, gas concentrations may be calculated precisely via Lambert–Beer's law.

For this measurement principle, long wavelength VCSELs are ideal light sources, as the single-mode emission is strongly (electro-)thermally tunable. Especially in the wavelength

range between 2 and 3 μm there are strong absorption lines of atmospheric pollutants or hazardous gases like CO, H_2S, HF, CH_4, CO_2, etc. Simultaneously, interference owing to H_2O absorption remains relatively low. The GaSb-based material system (AlGaIn)(AsSb) is the material of choice for achieving highly reliable devices in that spectral region. Edge emitters have already proven application suited and address a wavelength range between 2 and 3.36 μm [4, 5]. For single-mode operation, distributed feedback (DFB) lasers have been realized [6, 7]. However, their current tuning range is rather low and production costs are high. The research on electrically pumped VCSELs based on GaSb is still at a preliminary stage. Mesa constricted devices, emitting between 2.2 and 2.63 μm, have been presented in [8, 9], and continuous-wave (cw) devices at 2.33 μm in [10, 11]. In this paper, we give detailed information on the device fabrication, design and results of cw operating VCSELs emitting single-mode at 2.4 and 2.6 μm. At these wavelengths, for instance, absorption lines of CH_4 and HF are present. The devices incorporate a buried tunnel junction (BTJ) for electrical and optical confinement.

2. BTJ

Semiconductor interband lasers are usually made of a *p*-*i*-*n*-double-hetero-junction where holes and electrons recombine in an intrinsic (*i*) region. *n*-doped material usually offers higher electrical conductivity than *p*-type one, as the majority carriers have higher mobilities. Additionally, the optical losses are smaller in *n*-type semiconductors because the *p*-type ones suffer from intervalence band absorption. Therefore, it is beneficial to reduce the amount of *p*-doped layers in a VCSEL. The use of tunnel-junctions in VCSELs has already been described in the literature [12, 13], offering the advantage of substituting *p*-type layers by *n*-type ones by combining highly doped p^+- and n^+-layers. In this case, tunneling becomes a major process and electrons may move from the valence band of the p^+-doped layer to the conduction band of the n^+-doped layer leaving holes. In an external field, these carriers are separated, creating a current. By placing this junction in a node of the optical field close to the active region, most of the *p*-doped material in the device may be substituted by *n*-doped material. In the GaSb-based material system, the use of a p^+-GaSb and lattice-matched n^+-$InAs_{0.91}Sb_{0.09}$ type III heterojunction has been reported to show low-resistive ($2.4 \times 10^{-6}\ \Omega cm^2$) ohmic characteristics [15, 16]. Both layers can be doped with Si, being an amphoteric dopant. This is particularly beneficial, as no dopant diffusion problems occur [17] and the growth is easy.

For efficient device performance, VCSELs usually incorporate a means of confining the current to the center of the device. In GaAs-based devices, this is usually achieved by selective lateral wet oxidation of an Al-containing layer [14], which is strongly reducing its electrical conductivity and therefore forming a ring contact to the active region. However, in GaSb-based devices, oxidation is difficult to realize. Salesse *et al* [18] and Meneou *et al* [19] studied wet chemical oxidation of AlAsSb layers on GaSb. However, a strong spacial expansion of the material leads to a strong mismatch or destruction of the material, and the remaining metallic Sb in the oxide may form a shunt path.

Using a structured BTJ, a very effective current confinement can also be achieved, as has already been shown for InP-based VCSELs [13]. By etching the n^+-doped layer in the above described tunnel junction and subsequently overgrowing the structure by low-doped material, a blocking p^+n-junction is formed. In GaSb-based VCSELs, a first growth run will end up with the tunnel junction layers. Then circular or elliptical mesas will be defined by standard UV-lithography and subsequent etching of the outer InAsSb-layer. In a second growth run, *n*-GaSb

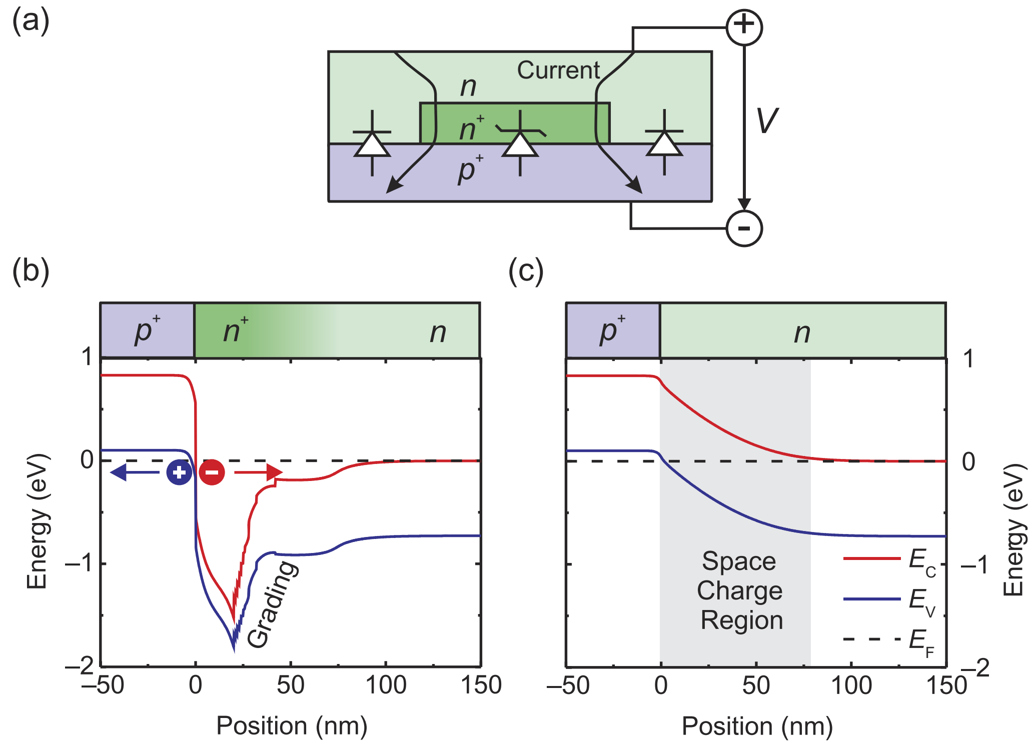

Figure 1. (a) Schematic view of BTJ with current flow. (b) Band diagram of p^+-GaSb/n^+-InAsSb/grading/n-GaSb tunnel junction. (c) Band diagram of blocking p^+-GaSb/n-GaSb diode. All band diagrams have been calculated with SimWindows 1.5.0 (www.simwindows.com) using the material parameters from [20].

($n = 1.5 \times 10^{17}\,\mathrm{cm}^{-3}$) is deposited, leading to the structure schematically shown in figure 1(a). Here, the current is confined to the center of the device, restricting the pumped diameter of the active region to the BTJ-diameter plus an extension caused by lateral carrier diffusion. Figures 1(b) and (c) display the band diagram of the conducting central and the blocking etched part of the BTJ, respectively. For better electrical conductivity and ohmic characteristics, a graded junction is introduced between the n^+-InAsSb and the n-GaSb layers. These grading layers are made of $(\mathrm{Ga}_x\mathrm{In}_{1-x})(\mathrm{As}_y\mathrm{Sb}_{1-y})$ with a homogeneously increasing Ga-content and decreasing In-amount. The As- and Sb-concentrations (y) are chosen in such a way that the layers are lattice-matched to the substrate. Further details can be found in [16].

Besides an effective current confinement, the BTJ concept also enables lateral waveguiding since the cavity length changes from the etched to the non-etched regions, as depicted in figure 2(a). The waveguiding properties can be investigated by using a simple effective index model developed by Hadley [21]. The resonator can be described similar to a glass fiber by using the effective indices in the central part $n'_{\mathrm{eff},1}$ and in the outer part $n'_{\mathrm{eff},2} = n'_{\mathrm{eff},1} - \Delta n'_{\mathrm{eff}}$. According to [21], this can be described by a shift in the resonator wavelengths $\Delta\lambda = \lambda_1 - \lambda_2$ in regions 1 and 2,

$$\frac{\Delta n'_{\mathrm{eff}}}{n'_{\mathrm{eff},1}} = \frac{\Delta\lambda}{\lambda_1}. \tag{1}$$

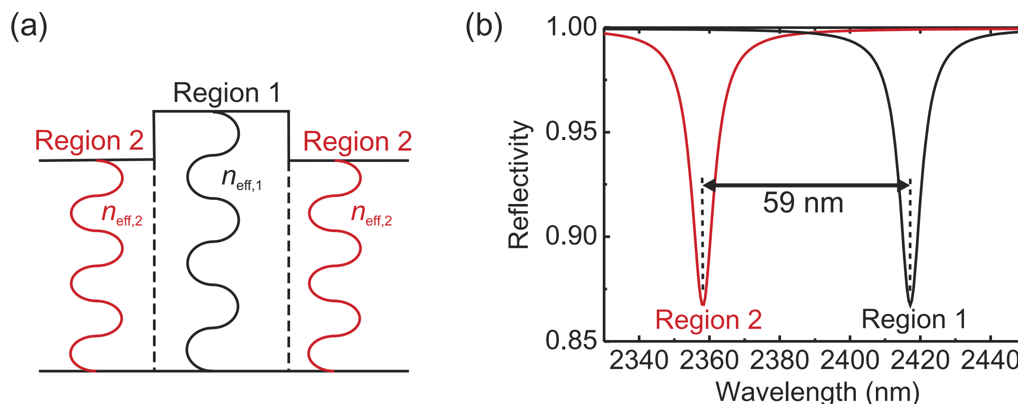

Figure 2. (a) Schematic field intensity profile in a VCSEL with differing cavity lengths. Region 1 depicts the inner region of the VCSEL, region 2 the outer part with etched tunnel junction layers. (b) Calculated reflectivity spectrum of VCSEL with lasing modes for regions 1 and 2.

Figure 2(b) displays the calculated reflectivity spectra for regions 1 and 2 for a VCSEL designed for emission at 2.42 μm. The dips correspond to the resonance modes in the regions 1 and 2. As the above mentioned grading layers must be included in the non-etched part of the tunnel junction for better electrical conductivity, the difference in physical length between regions 1 and 2 is rather high with 72 nm, leading to strongly separated cavity resonances of 59 nm. With equation (1) this gives a relative change of the effective indices of $\Delta n'_{\mathrm{eff}}/n'_{\mathrm{eff},1} = 2.4\%$, showing that VCSELs incorporating this tunnel junction are strongly index-guided. This will lead to multimode behavior even for small aperture diameters. For improving the single-mode VCSELs, the step has to be reduced. In a first approach, it has already been decreased to 52 nm for a 2.6 μm device (see section 4.2), leading to a relative effective index step of 1.3%.

3. Device design and fabrication

3.1. Device structure

Figure 3 shows the schematic structure of the GaSb-based BTJ-VCSEL. The cavity is formed by two distributed Bragg reflectors (DBRs) embedding a layer structure of an optical thickness of 3λ. The bottom mirror is epitaxially grown, consisting of 24 pairs of alternating, lattice-matched $AlAs_{0.09}Sb_{0.91}/GaSb$ layers. On top of the device, a dielectric mirror is used, made of amorphous Si and SiO_2. For the 2.4 μm laser, the active region consists of five 11 nm thick $Ga_{0.63}In_{0.37}As_{0.11}Sb_{0.89}$ quantum wells (QWs), embedded in 8 nm thick $Al_{0.33}Ga_{0.67}As_{0.03}Sb_{0.97}$ barriers. The QWs are compressively strained by 1.6%. In order to decrease the transition energy for higher emission wavelength, one has to increase the In-concentration. In this work, 10 nm thick $Ga_{0.57}In_{0.43}As_{0.14}Sb_{0.86}$ QWs embedded in pure GaSb-barriers have been used for 2.6 μm emission. This active region has been proven successfully in edge emitting lasers [24] and has therefore been adapted to VCSELs.

On top of the active region, the BTJ is placed, confining the current to the center of the device. In order to achieve low resistive lateral current flow, several current spreading layers are

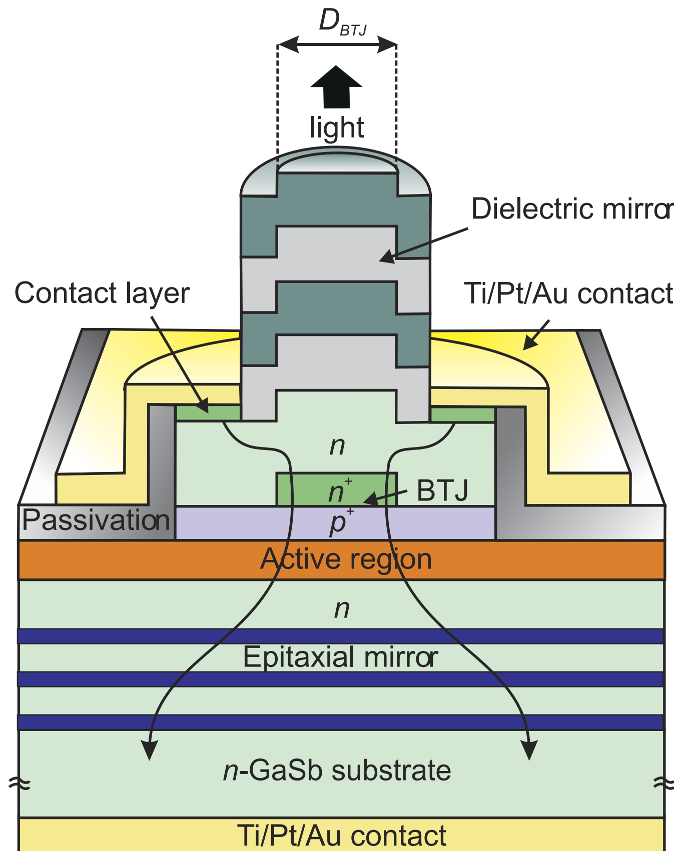

Figure 3. Schematic structure of GaSb-based BTJ-VCSEL.

added in between the BTJ and the top contacts. The lateral spreading resistance of the GaSb layers with thickness d can be approximated by [22]

$$R = \frac{\rho_{\mathrm{GaSb}}}{2\pi d} \ln \frac{r_2}{r_1} = \frac{1}{eN_{\mathrm{D}}\mu} \frac{1}{2\pi d} \ln \frac{r_2}{r_1}, \quad (2)$$

where ρ_{GaSb} denotes the specific resistivity, r_1 the radius of the tunnel junction aperture, r_2 the inner radius of the contact ring, e the elementary charge, N_{D} the doping concentration and μ the carrier mobility. In the device, a modulation doping is applied in a way that highly doped layers remain in the node of the optical field. Thus, both free-carrier absorption losses and lateral electrical resistance can be reduced. The thickness of the current spreading layers are chosen as a trade-off between optical and electrical properties. Using typical values for the GaSb-based VCSEL, such as an average doping of about $8 \times 10^{17}\,\mathrm{cm}^{-3}$, electron mobility of $3000\,\mathrm{cm}^2\,\mathrm{Vs}^{-1}$, $d = 1\,\mu$m, $r_2 = 6\,\mu$m and $r_1 = 3\,\mu$m, the lateral resistance calculates to about $3\,\Omega$.

3.2. Fabrication

The growth of the structure is performed by molecular beam epitaxy (MBE) on a Varian Gen-II system equipped with solid source cells. As already mentioned, the complete growth consists of two MBE-runs because of the intermediate structuring of the tunnel junction. The first run starts with the growth of the epitaxial DBR, a few current and heat spreading layers, the active region and the tunnel junction including the grading layers mentioned in section 2. Then, the

tunnel junction layers are structured by selective wet-chemical etching based on KNa–tartaric acid [23] and subsequent dry-chemical etching of InAsSb in a $CH_4/H_2/N_2$ plasma. Due to residual resist, possible polymer contamination after the dry etching and the strong oxidation tendency of GaSb-based materials [25], a special surface treatment is necessary in order to achieve clean surface conditions for the second growth run. This technique is based on the removal of oxides by HCl and subsequent rinsing in deionized water, forming a defined oxide layer with a slight depletion of antimony [26]. As the oxide will grow quickly after re-exposure to air, the sample is immediately loaded into the MBE chamber, where the intentionally formed oxide layer is removed by atomic hydrogen cleaning [27].

The overgrowth consists of the modulation-doped *n*-GaSb current spreading layers and a highly doped ($n = 1 \times 10^{20}\,\mathrm{cm}^{-3}$) InAsSb-layer for the metal–semiconductor contact. Note that unannealed contacts on *n*-GaSb are highly resistive and show non-ohmic characteristics due to the valence band pinning and the Te doping limit of only $2 \times 10^{18}\,\mathrm{cm}^{-3}$. However, the use of InAsSb with its low bandgap and a Ti/Pt/Au metal contact leads to ohmic contacts with specific contact resistances of $\rho = 5 \times 10^{-6}\,\Omega\,\mathrm{cm}^2$ [28, 29] without annealing. This is particularly important due to the blueshift effect of the active material (see section 3.3.3).

The device processing is continued by etching the mesa with a Cl_2-based reactive ion etching. The mesa sidewall is then passivated with 200 nm thick sputtered SiO_2 and a subsequent lift-off process to open the mesa top side. After wet chemical etching of the contact layer in the central part of the device with a citric acid-based solution [23], the metal–semiconductor contacts are formed. For this, the wafer is dipped into HCl to remove oxides and immediately in a $(NH_4)_2S$-based solution to prevent further formation of oxides. This procedure terminates the dangling bonds at the contact surface in the form of S–In, S–As and S–Sb. After promptly loading the wafer into the metallization chamber, 3 nm Ti for adhesion, 40 nm Pt as diffusion barrier and finally 300 nm Au are evaporated. Further details on the contact technology can be found in [29]. The backside contact is also realized by Ti/Pt/Au evaporation.

Finally, the device processing is completed with the e-beam evaporation of the dielectric mirror and subsequent structuring by a lift-off technique. This mirror type is chosen since the growth of an epitaxial DBR in a second growth step shows insufficient optical properties.

3.3. Optical properties

3.3.1. DBRs. Owing to the short gain region in a vertical cavity laser, highly reflective mirrors are necessary (reflectivity $R > 99\%$). DBRs, being made of quarterwave layers with alternating high and low refractive index n', fulfill this condition. In the (AlGaIn)(AsSb) material system, lattice-matched $AlAs_{0.09}Sb_{0.91}/GaSb$ offers a high refractive index contrast of $\Delta n' \approx 0.65$, yielding high reflectivity at a reasonable number of layer pairs. Free carrier absorption due to dopant carriers is commonly known as the main absorption mechanism in *n*-doped semiconductors at long wavelengths, as it is proportional to λ^2 and to the carrier density n [30]. However, because of the current flow, the bottom mirror has to be *n*-doped. Therefore, a trade-off is necessary. Figure 4 shows calculated mirror reflectivities versus the number of layer pairs for different doping levels. As can be seen, the reflectivity versus number of layer pairs characteristics is saturating for doped layers due to absorption losses. Therefore, a rather low bulk carrier density of $n = 5 \times 10^{17}\,\mathrm{cm}^{-3}$ and 24 pairs are chosen, yielding a reflectivity of nearly 99.9%. A further increased layer pair number at this doping level would not increase the mirror reflectivity significantly.

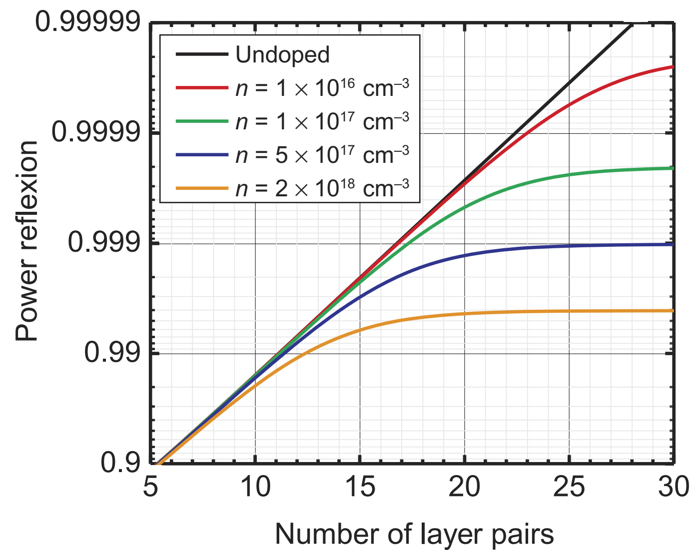

Figure 4. Power reflectivity of an n-doped $AlAs_{0.09}Sb_{0.91}/GaSb$ DBR for 2.4 μm emission wavelength for different number of layer pairs at various carrier densities n.

However, the largest contribution to electrical resistance is given by the high hetero-interface barrier at the GaSb/AlAsSb interface due to large space charge regions. In order to improve the electrical properties of interfaces, usually gradings or super-lattice layers are introduced. In this work, a digital superlattice consisting of ten periods of 1 nm AlSb and 1 nm GaSb has been used, leading to a reduction of the specific resistance per interface by about 58% ($1.5 \times 10^{-5}\,\Omega\,\text{cm}^2$ instead of $3.6 \times 10^{-5}\,\Omega\,\text{cm}^2$ at $1\,\text{kA}\,\text{cm}^{-2}$, see [31]). Due to the higher doping of these layers, the peak reflectivity of a 24-pair mirror in the device is further reduced to 99.8%.

The upper DBR is made of dielectrics. In this work, either three or four pairs of $\lambda/(4n')$ thick amorphous Silicon/SiO_2 layers have been used. These materials offer a high index contrast of about $\Delta n' = 2.0$, so that a peak reflectivity of 99.8 or 99.5% can be achieved for four or three pairs, respectively. At the same time, optical absorption losses at wavelengths above 2 μm are kept very low.

3.3.2. Cavity design. An appropriate cavity design should aim for low threshold gain and optical losses. By placing the active region in a field anti-node, the longitudinal overlap of the field intensity with the active region can be maximized up to a theoretical limit of $\Gamma_r = 2$ for a very thin QW. Here, Γ_r denotes the relative confinement factor, see [32]. In the case of five 11 nm thick QWs with 8 nm barriers (see section 3.1), the maximum achievable relative confinement factor is calculated to 1.8, assuming optimal positioning. Also, highly absorbing layers shall be placed in a field node, in order to contribute only slightly to the total losses ($\Gamma_r \to 0$). Therefore, the highly absorbing BTJ layers, where fundamental and high free-carrier absorption take place due to the low bandgap and high doping levels, respectively, are placed in the nearest field node to the active region. All current spreading layers are also situated in field nodes.

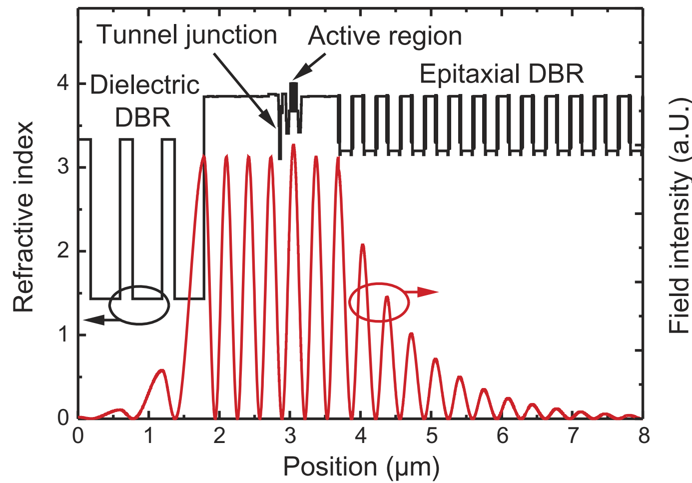

Figure 5. Standing wave pattern and refractive index distribution in GaSb-based BTJ-VCSEL.

Taking the design criteria of section 3.1 into account, a physical thickness of $3\lambda/n'$ is chosen for the structure in between the mirrors. The overall effective cavity length L_{eff} is given by

$$L_{\mathrm{eff}} = L_{\mathrm{cav}} + L_{\mathrm{bot}} + L_{\mathrm{top}}, \tag{3}$$

where L_{cav} describes the physical length of the cavity in between the mirrors and L_{bot} and L_{top} the effective penetration depths (1/e decay) of the optical field into the bottom and top DBRs, respectively. For the presented structure, the overall cavity length adds to about 3.3 μm. Figure 5 shows a one-dimensional calculation of the field distribution in the device.

3.3.3. Active region. The emission wavelength of a VCSEL is defined by the cavity length. Due to the short effective cavity length, usually only one longitudinal mode can reach threshold, making these devices inherently longitudinally single-mode. Both cavity resonance and gain maximum move to higher wavelengths if the temperature is increased. While the cavity resonance is mainly determined by the temperature dependence of the refractive indices [33], the shift of the gain maximum is given by the dependence of the bandgap energy. The rates for GaSb-based VCSELs are about 0.25 and 1 nm K^{-1} for the cavity resonance and the gain maximum, respectively. Additionally, the peak net gain deteriorates at higher temperature due to broadening and increased non-radiative Auger recombination, which is known as a main loss mechanism in long wavelength devices [34]. If the peak gain and cavity resonance were aligned in the passive state, the applied electrical power would create a temperature rise due to ohmic heating and the gain maximum and cavity resonance would diverge. Therefore, one usually applies a certain blueshift to the active region gain with respect to the cavity resonance so that the optimum relative alignment of gain peak and cavity resonance is given at an elevated cavity temperature. Due to the strong (cubic) dependence of Auger recombination on carrier density N, this alignment becomes even more important in long wavelength VCSELs to keep N within reasonable limits.

On the other hand, for designing the QW gain section in the GaInAsSb material, a commonly known blueshift during exposure to high temperatures has to be taken into account. As described in [35], a blueshift of up to 61 meV occurs when the material is annealed at

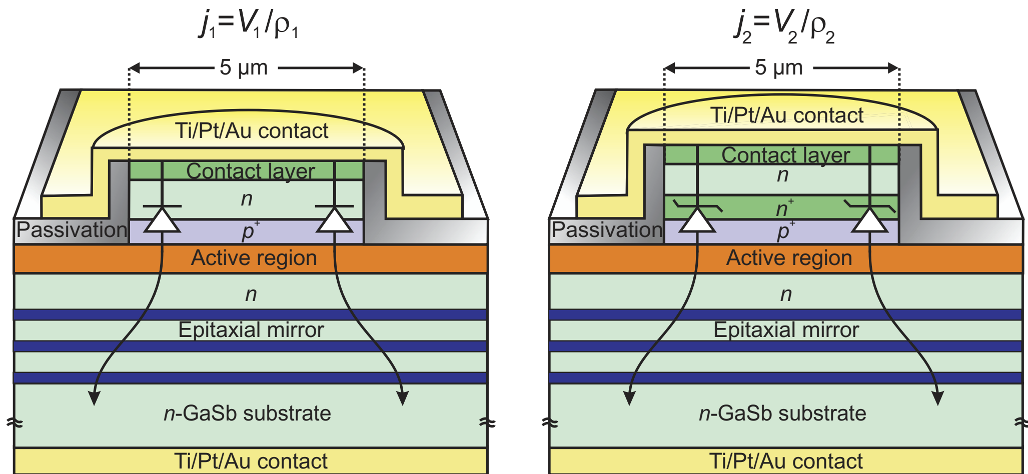

Figure 6. Structures included on the VCSEL wafer for the determination of the blocking ratio B. ρ denotes the specific resistance.

temperatures exceeding 430 °C. After structuring the BTJ, more than 530 °C are applied to the structure during the cleaning procedure and the overgrowth, resulting in a significant blueshift. Therefore, QW layers with a higher In concentration have to be grown to reach the target peak gain energy in the final device.

4. Results

VCSELs emitting around 2.4 and 2.6 μm were fabricated as described in section 3.2. All devices were tested on-wafer on a temperature controlled copper heat sink in the range of −20 to 100 °C. *L–I*-characteristics were measured with a Peltier-cooled InAs detector. For the recording of the spectra a Vertex 70 FTIR (Bruker Optics GmbH) equipped with a liquid nitrogen cooled InSb detector was used.

4.1. VCSELs emitting at 2.4 μm

GaSb-based single-mode VCSELs emitting around 2.33 μm with a maximum output power of typically 50 μW have already been presented [10]. On the way toward achieving higher emission wavelength, the design has been modified by slightly thicker DBRs and cavity thicknesses. Moreover, the reflectivity of the top DBR has been decreased to 99.5% by using three instead of four a-Si/SiO_2 layer pairs. This will increase the output power.

For superior device performance, the BTJ has to confine the current within the center of the device efficiently. The technological realization depends on the successful cleaning procedure, as described in section 3.2. The performance can be described by the current density blocking ratio B, defined as

$$B = \frac{j_2}{j_1}, \tag{4}$$

where j_2 and j_1 describe the current densities in the non-etched and the etched region of the BTJ, respectively. For the determination of that ratio, special test structures are implied in the mask, as shown in figure 6. From the measured *I–V* characteristics, the blocking ratio can be determined

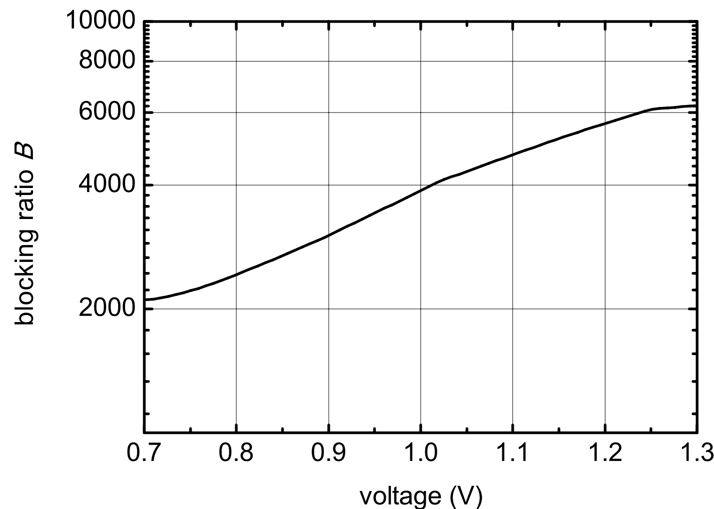

Figure 7. Measured blocking ratio B on a 2.4 μm VCSEL wafer.

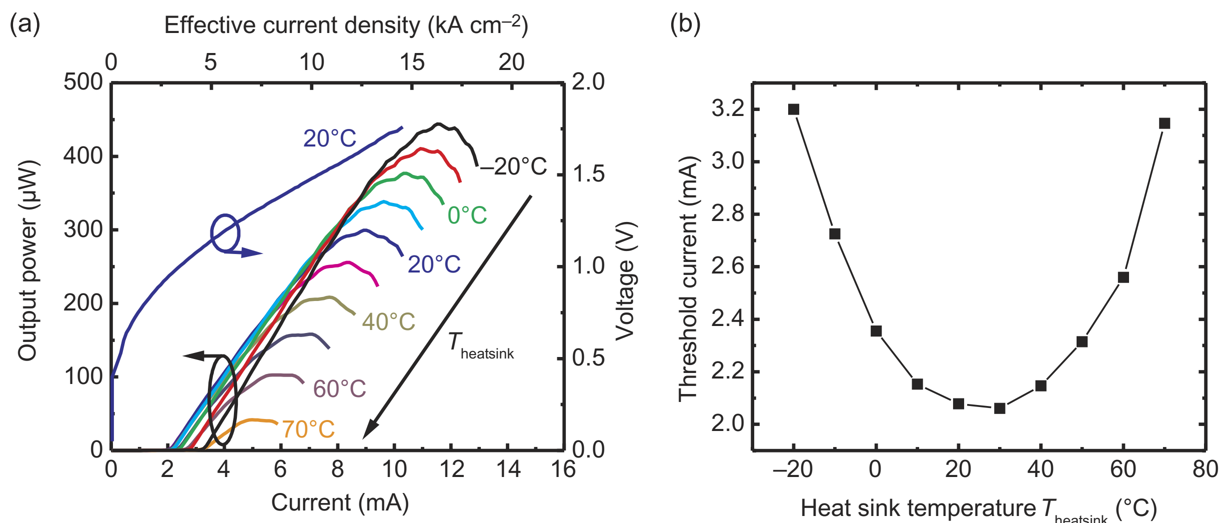

Figure 8. (a) Plot of cw L–I-characteristics of a GaSb-based VCSEL for 2.4 μm emission with 5.5 μm aperture diameter in a temperature range from −20 to 70 °C and I–V-characteristics at 20 °C (b) Threshold current versus heat sink temperature behavior of the VCSEL.

by dividing the currents at a fixed voltage as shown in figure 7. Values larger than 2000 are obtained for voltages >0.8 V. A typical ratio of the areas defined by the BTJ and the mesa, i.e. the areas with tunneling and blocking properties, is approximately 1 : 15. Accordingly, the current is perfectly confined to the center of the device. Due to not negligible series resistances in the test structures resulting from the DBR and the metal–semiconductor contacts, the true blocking ratio of the tunnel junction layers is even larger, as the series resistance is strongly increasing j_2 at a particular voltage.

Figure 8(a) shows temperature-dependent L–I–V-characteristics of a VCSEL with an aperture diameter of 5.5 μm. Continuous-wave operation has been achieved up to a stage

temperature of 70 °C. The differential resistance for voltages above 1.2 V is 87 Ω, proving good electrical device performance leading to reasonable device heating. A maximum output power of 440 μW has been measured at −20 °C.

Figure 8(b) shows the threshold current behavior versus heatsink temperature of this laser. At 30 °C, the threshold current reaches a minimum value of 2.06 mA. This value corresponds to an effective threshold current density of 2.9 kA cm^{-2}, if a lateral carrier diffusion of 2 μm on each side is taken into account. As described in section 3.3.3, the gain maximum shifts more strongly with temperature than the cavity resonance. Therefore, the optimum relative alignment is given at a specific heat sink temperature. It can be obtained by producing edge-emitting lasers incorporating the same active region than the VCSEL. The temperature dependence of an edge-emitting laser is given by the characteristic temperature T_0,

$$j_{\mathrm{th}} \propto \exp \frac{T}{T_0}, \tag{5}$$

where j_{th} is the threshold current density and T is the temperature of the active region. Measurements on edge emitting lasers give the active material's $T_0 \approx 60$ K, describing the gain peak shift with temperature. In the VCSEL, T_0 depends on the ambient temperature. Although the temperature dependence of the threshold currents of VCSELs depend on many parameters, at least the temperature where optimum mode-gain alignment is given may be estimated out of the comparison to the edge-emitting laser. Taking into account a slight heating of the active region in the VCSEL of about 5 K, one can estimate it by calculating the temperature-dependent characteristic temperature out of figure 8(b). At $T_{\mathrm{heatsink}} \approx 60$ °C, the VCSEL's characteristic temperature is the same as in the edge emitting lasers.

In the same temperature range, the previously published devices [10] only showed increasing threshold. In this study, the same active region has been used, but the cavity thickness has been increased. Therefore, the emission wavelength shifts from about 2.33 to 2.41 μm. Thereby, the offset between cavity mode and gain maximum is optimized, yielding a higher maximum operation temperature. The higher threshold current density compared to [10] can be explained by the increased mirror losses, as the top mirror reflectivity has been decreased. By that means, the output power could be increased by a factor of five.

Figure 9 shows cw spectra of the device at 20 °C. By changing the driving current, the emission wavelength is tunable in a range of 8 nm from 2.414 to 2.422 μm. Single-mode operation with a side-mode suppression ratio (SMSR) >20 dB over the whole tuning range has been achieved. The linewidth is attributed to the limited measurement accuracy of the FTIR. The tuning characteristics are shown in figure 10. By current-induced self-heating, a tuning efficiency of about 1.22 nm mA^{-1} is measured. By changing the heat sink temperature between −20 and 60 °C at a constant bias current of 5 mA, a wavelength range of 2406–2425 nm can be reached, corresponding to a tunability rate of 0.24 nm K^{-1}. Due to the large accessible wavelength range with single-mode operation, this device is ideally suited for gas sensing applications. Several gas absorption lines may be scanned at a time by tuning the emission wavelength.

By using the (electro-)thermal tunability rates $\partial\lambda/\partial P$ and $\partial\lambda/\partial T$ at constant heatsink temperature and electrical power P, respectively, one can estimate the thermal resistance R_{th} of the device with

$$R_{\mathrm{th}} = \frac{\partial\lambda/\partial P}{\partial\lambda/\partial T}. \tag{6}$$

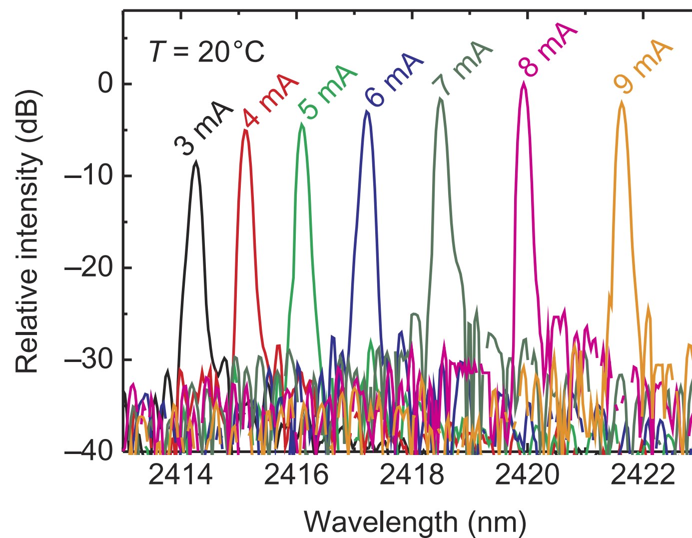

Figure 9. Current-dependent cw spectra of the VCSEL from figure 8 at 20 °C.

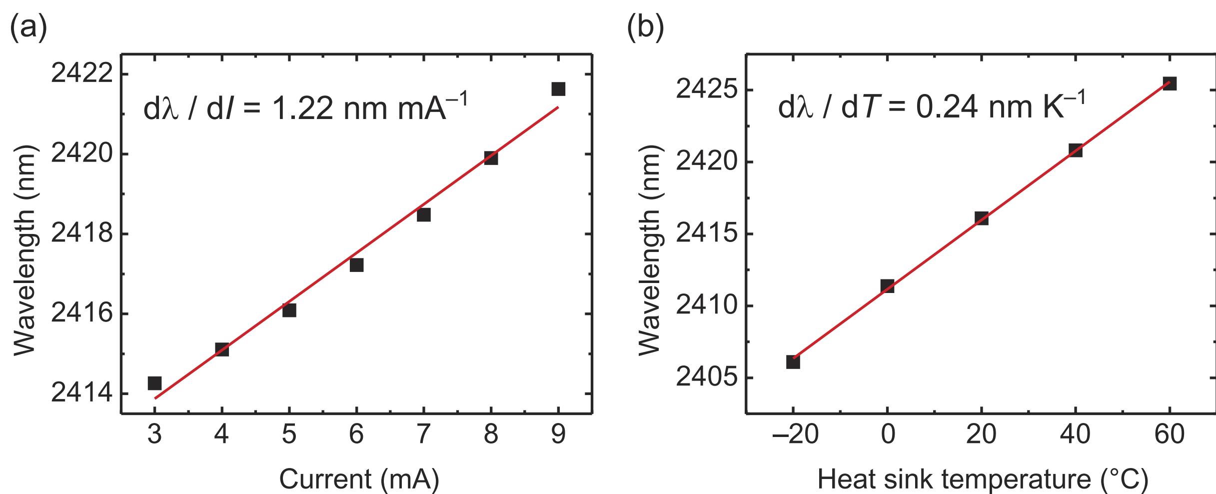

Figure 10. (a) Current tunability of the GaSb-based VCSEL from figure 8 at 20 °C. (b) Temperature tunability at constant current of 5 mA.

By considering the applied voltage, the power tunability calculates to 0.63 nm mW^{-1}, leading to a thermal resistance of 2625 K W^{-1}. This value demonstrates the considerable thermal conductivity of the epitaxial DBR and a good thermal design of the laser. At threshold ($I_{\mathrm{th}} = 2$ mA and $U_{\mathrm{th}} = 0.93$ V at 30 °C), the additional heating of the active region can be estimated to be about 5 K, justifying the above mentioned assumption for the determination of the optimum mode-gain alignment.

In figure 11(a), far-field measurement of the VCSEL at room temperature and a bias current of 7 mA is shown, yielding fundamental mode emission. The half-width is $\approx 20^\circ$.

Devices similar to the presented ones have already been proven to be application suited. By using the large tunability, CO and CH_4 could be measured simultaneously [36]. By improving the relative position of active region and tunnel junction with respect to the optical field, it is

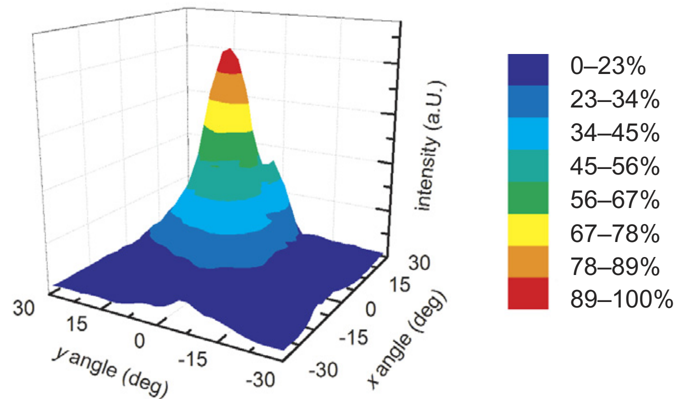

Figure 11. Far-field measurement of the 2.4 μm VCSEL from figure 8 at room temperature and 7 mA, yielding fundamental mode emission.

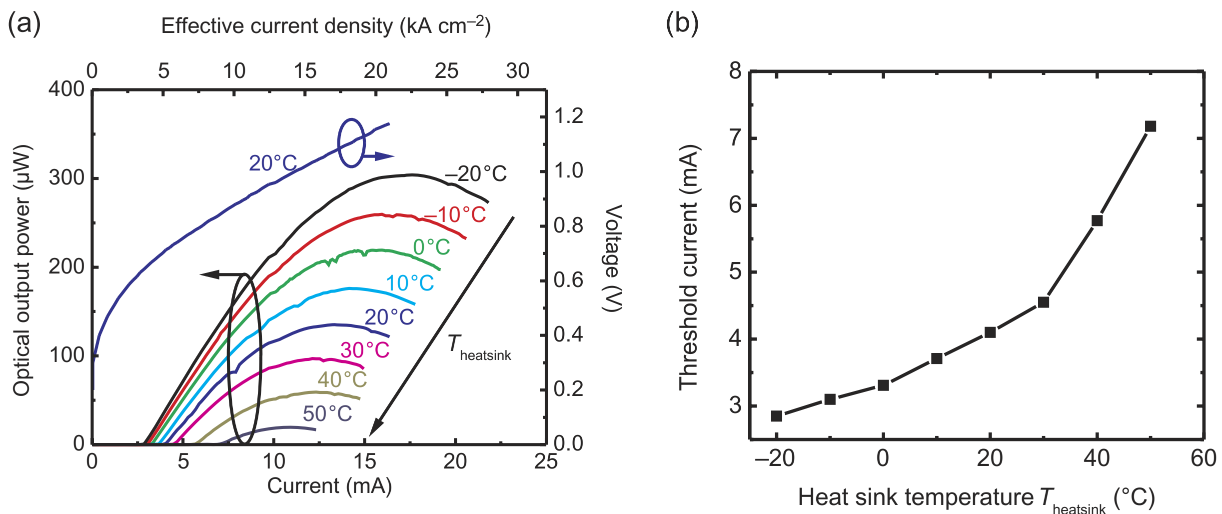

Figure 12. (a) Plot of cw L–I–V-characteristics of the GaSb-based VCSEL for 2.6 μm emission with 6 μm aperture diameter in a temperature range from −20 to 50 °C. (b) Threshold current versus heat sink temperature behavior.

expected that both output power and efficiency of the devices will further improve in future. Furthermore, the active region can be optimized concerning number of QWs, barrier thickness and material composition.

4.2. VCSELs emitting at 2.6 μm

On the way toward longer wavelength emission, a device for 2.6 μm was designed. The structure is the same as for the above described VCSELs, adapted for the higher wavelength emission. In order to reduce mirror losses, a four pair dielectric mirror was evaporated. The measured blocking ratios are comparable to the ones presented for the 2.4 μm devices. Continuous-wave L–I–V-characteristics of a device with 6 μm aperture diameter are shown in figure 12(a). Laser

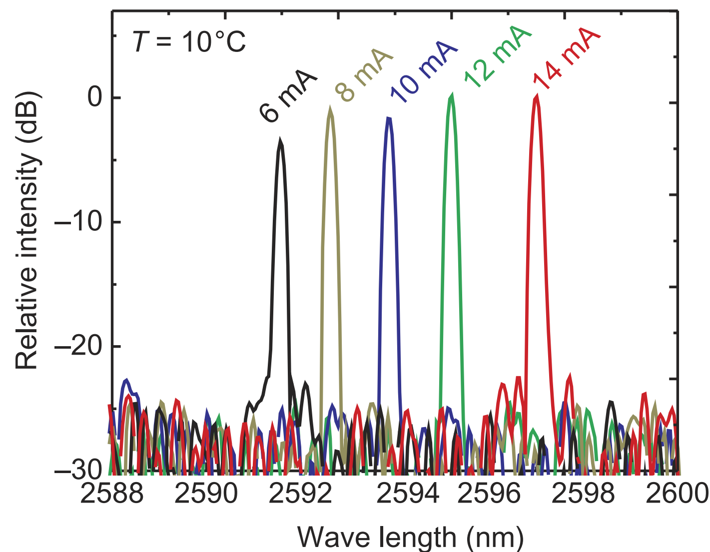

Figure 13. Plot of cw spectra of VCSEL from figure 12 for different driving currents at a heatsink temperature of 10 °C.

emission up to 50 °C has been achieved. The differential resistance at voltages >0.9 V is ≈35 Ω. This improvement with respect to the presented 2.4 μm VCSEL can partly be explained by the increased BTJ diameter. Furthermore, the thicker current spreading layers lead to higher electrical conductivity and the active region has been improved by using barriers with smaller bandgap (see section 3.3.3).

The threshold current versus heat sink temperature behavior is shown in figure 12(b). As can be seen, the threshold current does not reach its minimum value in the given temperature range. Therefore, significant improvement can be expected by improving the relative alignment of the cavity resonance and the spectral gain.

Single-mode emission with a SMSR >20 dB over the whole current range could be found at a wavelength of around 2.6 μm. To the best of our knowledge, this is the first cw, single-mode room temperature operation of electrically pumped VCSELs at 2.6 μm ever presented. At 10 °C, the device can be tuned mode-hop free over a wavelength range of 7 nm, corresponding to 0.62 nm mA^{-1}. By changing the heat sink temperature, a tuning rate of 0.26 nm K^{-1} is achieved. With equation (6), the thermal resistance calculates to 1923 K W^{-1}, being smaller than for the presented 2.4 μm VCSEL due to the larger BTJ diameter.

5. Conclusion and outlook

In this paper, a device concept for an electrically pumped GaSb-based VCSEL has been presented. The devices incorporate an epitaxial DBR as bottom mirror, grown on GaSb-substrate, a QW active region with quaternary GaInAsSb and a dielectric DBR as top reflector. For electrical and optical confinement, a BTJ is used. Two devices have been presented, both emitting cw with threshold currents of only several milliamperes. The emission wavelengths are 2.4 and 2.6 μm. The lasers emit longitudinally as well as transversely in the single fundamental mode and are tunable over several nanometers. Therefore, they are very well suited

for gas sensing applications by TDLAS. Further improvement of the devices will continue by optimizing the cavity design and the active regions. Lifetime measurements are currently under investigation. After more than 2000 h of operation, no device failures have occurred. The presented device concept may easily be applied to lasers emitting at even longer wavelengths.

Acknowledgments

We gratefully acknowledge measurement support by VERTILAS GmbH. This work has been financially supported by the European Union via NEMIS (contract no. FP6-2005-IST-5-031845), the German Federal Ministry of Education and Research via NOSE (contract no. 13N8772) and the Excellence Cluster 'Nanosystems Initiative Munich (NIM)'.

References

[1] Hall R N, Fenner G E, Kingsley J D, Soltys T J and Carlson R O 1962 *Phys. Rev. Lett.* **9** 366–8
[2] Iga K 2000 *IEEE J. Sel. Top. Quantum. Electron.* **6** 1201–15
[3] Soda H, Iga K, Kitahara C and Suematsu Y 1979 *Japan J. Appl. Phys.* **18** 2329–30
[4] Lin C, Grau M, Dier O and Amann M C 2004 *Appl. Phys. Lett.* **84** 5088
[5] Shterengas L, Belenky G, Hosoda T, Kipshidze G and Suchalkin S 2008 *Appl. Phys. Lett.* **93** 011103
[6] Hummer M, Rossner K, Lehnhardt T, Müller M, Forchel A, Werner R, Fischer M and Koeth J 2006 *Electron. Lett.* **42** 583–4
[7] Seufert J, Fischer M, Legge M, Koeth J, Werner R, Kamp M and Forchel A 2004 *Spectrochim. Acta* A **60** 3243–7
[8] Ducanchez A, Cerutti L, Grech P and Genty F 2008 *IEEE Photonics Technol. Lett.* **20** 1745–7
[9] Ducanchez A, Cerutti L, Grech P, Genty F and Tournié E 2009 *Electron. Lett.* **45** 265–7
[10] Bachmann A, Kashani-Shirazi K and Amann M C 2008 *IEEE 21st Semiconductor Laser Conf.* pp 39–40
[11] Bachmann A, Lim T, Kashani-Shirazi K, Dier O, Lauer C and Amann M C 2008 *Electron. Lett.* **44** 202–3
[12] Starck C 1999 *Lasers and Electro-Optics Society 12th Annu. Meeting* vol 1, pp 139–40
[13] Ortsiefer M, Shau R, Böhm G, Köhler F, Abstreiter G and Amann M C 2000 *Japan J. Appl. Phys.* **39** 1727–9
[14] Huffaker D L, Deppe D G and Kumar K 1994 *Appl. Phys. Lett.* **65** 97–9
[15] Dier O, Lauer C and Amann M C 2006 *Electron. Lett.* **42** 419–20
[16] Dier O, Sterkel M, Grau M, Lin C, Lauer C and Amann M C 2004 *Appl. Phys. Lett.* **85** 2388–9
[17] Dier O, Grau M, Lauer C, Lin C and Amann M C 2005 *J. Vac. Sci. Technol.* B **23** 349–53
[18] Salesse A *et al* 2000 *Appl. Surf. Sci.* **161** 426–33
[19] Meneou K, Lin H C and Cheng K Y 2004 *J. Appl. Phys.* **95** 5131–6
[20] Vurgaftman I, Meyer J R and Ram-Mohan L R 2001 *J. Appl. Phys.* **89** 5815–75
[21] Hadley G R 1995 *Opt. Lett.* **20** 1483–5
[22] Lauer C, Ortsiefer M, Shau R, Rosskopf J, Böhm G, Meyer R and Amann M C 2004 *Phys. Status Solidi* c **1** 2183–209
[23] Dier O, Lin C, Grau M and Amann M C 2004 *Semicond. Sci. Technol.* **19** 1250–3
[24] Kashani-Shirazi K, Bachmann A, Arafin S, Vizbaras K and Amann M C 2009 *Conf. on Lasers and Electro-Optics 2009 (CLEO)*
[25] Robinson J A and Mohney S E 2004 *J. Appl. Phys.* **96** 2684–8
[26] Liu Z Y, Hawkins B and Kuech T F 2003 *J. Vac. Sci. Technol.* B **21** 71–7
[27] Bell G R, Kaijaks N S, Dixon R J and McConville C F 1998 *Surf. Sci.* **401** 125–37
[28] Lauer C, Dier O and Amann M C 2006 *Semicond. Sci. Technol.* **21** 1274–7
[29] Arafin S, Bachmann A, Kashani-Shirazi K, Priyabadini S and Amann M C 2009 *Proc. Semiconductor and Integrated OptoElectronics (SIOE) Conf., IET Optoelectronics* to be published

[30] Soref R A and Lorenzo J P 1986 *IEEE J. Quantum Electron.* **22** 873–9
[31] Dier O, Reindl C, Bachmann A, Lauer C, Lim T, Kashani-Shirazi K and Amann M C 2008 *Semicond. Sci. Technol.* **23** 025018
[32] Corzine S W, Geels R S, Scott J W, Yan R H and Coldren L A 1989 *J. Quantum Electron.* **25** 1513–24
[33] Yu P and Cardona M 1970 *Phys. Rev.* B **2** 3193–7
[34] Knowles G, Fehse R, Tomic S, Sweeney S J, Sale T E and Adams A R 2003 *J. Sel. Top. Quantum Electron.* **9** 1202–8
[35] Dier O, Dachs S, Grau M, Lin C, Lauer C and Amann M C 2005 *Appl. Phys. Lett.* **86** 151120
[36] Chen J, Hangauer A, Bachmann A, Lim T, Kashani K, Strzoda R and Amann M C 2009 *Conf. on Lasers and Electro-Optics 2009, Baltimore, MD*